

Emergence of a noncollinear magnetic state in twisted bilayer CrI₃

Yang Xu

Cornell University <https://orcid.org/0000-0003-4223-8677>

Ariana Ray

Cornell University

Yu-Tsun Shao

Cornell University

Shengwei Jiang

Cornell University <https://orcid.org/0000-0001-5213-0139>

Daniel Weber

Karlsruhe Institute of Technology <https://orcid.org/0000-0003-4175-9278>

Joshua Goldberger

The Ohio State University

Kenji Watanabe

National Institute for Materials Science <https://orcid.org/0000-0003-3701-8119>

Takashi Taniguchi

National Institute for Materials Science, Tsukuba, Ibaraki <https://orcid.org/0000-0002-1467-3105>

David Muller

Cornell University <https://orcid.org/0000-0003-4129-0473>

Kin Fai Mak (✉ kfaimak@gmail.com)

Cornell University <https://orcid.org/0000-0002-5768-199X>

Jie Shan

Cornell University <https://orcid.org/0000-0003-1270-9386>

Research Article

Keywords: magnetic crystals, memory storage, magnetic states

Posted Date: May 25th, 2021

DOI: <https://doi.org/10.21203/rs.3.rs-533063/v1>

License:   This work is licensed under a Creative Commons Attribution 4.0 International License.

[Read Full License](#)

Version of Record: A version of this preprint was published at Nature Nanotechnology on November 29th, 2021. See the published version at <https://doi.org/10.1038/s41565-021-01014-y>.

Emergence of a noncollinear magnetic state in twisted bilayer CrI₃

Yang Xu^{1,2}, Ariana Ray¹, Yu-Tsun Shao¹, Shengwei Jiang¹, Daniel Weber³, Joshua E. Goldberger³, Kenji Watanabe⁴, Takashi Taniguchi⁴, David A. Muller^{1,5}, Kin Fai Mak^{1,5,6*}, Jie Shan^{1,5,6*}

¹School of Applied and Engineering Physics, Cornell University, Ithaca, NY, USA

²Beijing National Laboratory for Condensed Matter Physics, Institute of Physics, Chinese Academy of Sciences, Beijing, China

³Department of Chemistry and Biochemistry, The Ohio State University, Columbus, OH, USA

⁴National Institute for Materials Science, Tsukuba, Japan

⁵Kavli Institute at Cornell for Nanoscale Science, Ithaca, NY, USA

⁶Laboratory of Atomic and Solid State Physics, Cornell University, Ithaca, NY, USA

*Email: kinfai.mak@cornell.edu; jie.shan@cornell.edu

The emergence of two-dimensional (2D) magnetic crystals and moiré engineering of van der Waals materials has opened the door for devising new magnetic ground states via competing interactions in moiré superlattices ¹⁻⁹. Although a suite of interesting phenomena, including multi-flavor magnetic states ¹⁰, noncollinear magnetic states ¹⁰⁻¹³, moiré magnon bands and magnon networks ¹⁴, has been predicted in twisted bilayer magnetic crystals, nontrivial magnetic ground states have yet to be realized. Here, by utilizing the stacking-dependent interlayer exchange interactions in CrI₃ (Ref. ^{15,16}), we demonstrate in small-twist-angle CrI₃ bilayers a noncollinear magnetic ground state. It consists of antiferromagnetic (AF) and ferromagnetic (FM) domains and is a result of the competing interlayer AF coupling in the monoclinic stacking regions of the moiré superlattice and the energy cost for forming AF-FM domain walls. Above a critical twist angle of $\sim 3^\circ$, the noncollinear state transitions to a collinear FM ground state. We further show that the noncollinear magnetic state can be controlled by electrical gating through the doping-dependent interlayer AF interaction. Our results demonstrate the possibility of engineering new magnetic ground states in twisted bilayer magnetic crystals, as well as gate-voltage-controllable high-density magnetic memory storage.

Moiré superlattices built on twisted bilayers of van der Waals materials have presented an exciting platform for studying correlated states of matter with unprecedented controllability ⁷⁻⁹. In addition to graphene and transition metal dichalcogenide moiré materials ¹⁷, recent theoretical studies have predicted the emergence of new magnetic ground states in twisted bilayers of 2D magnetic crystals ¹⁰⁻¹⁴. These states are originated from the stacking-dependent interlayer exchange interactions in magnetic moiré superlattices. Two-dimensional CrI₃ (similarly CrBr₃ ¹⁸ and CrCl₃ ¹⁹), in which stacking-dependent interlayer magnetic ground states have been demonstrated by recent experiments ^{15,16}, is a good candidate for exploring moiré magnetism.

There is a one-to-one correspondence between the stacking structure and the magnetic ground state in CrI₃ bilayers: the monoclinic (M) phase supports an A-type AF ground state, in which two FM CrI₃ monolayers are antiferromagnetically coupled; and the rhombohedral (R) phase supports a FM ground state^{15, 16, 20, 21}. The interlayer FM exchange in the R-phase is substantially stronger than the AF exchange in the M-phase²⁰. The structure of the two phases can be viewed approximately as two monolayers displaced by a translation vector relative to each other with zero twist angle (Fig. 1b). In twisted bilayer CrI₃, the triangular moiré superlattice has both M- and R-stacking regions (Fig. 1a), and the competing interlayer AF and FM interactions can induce nontrivial magnetic ground states¹⁰⁻¹⁴. In particular, noncollinear magnetic ground states consisting of AF and FM domains (Fig. 1b) are expected, provided that the energy gain from forming the AF domains in the M-regions exceeds the energy cost from forming the domain walls. Since the energy gain scales with the area of the moiré unit cell whereas the energy cost scales with the moiré period, a noncollinear magnetic ground state is favored below a critical twist angle (or above a critical moiré period)¹⁰. This ideal picture could be modified in samples with very small twist angles, for instance, by atomic reconstruction²² that favors the most stable structure, the (FM) R-phase^{15, 16, 20}.

We fabricate twisted bilayer CrI₃ by the “tear-and-stack” method (Extended Data Fig. 1) that has been widely used in making twisted bilayer graphene samples²³⁻²⁵. A series of samples with varying target twist angle θ has been studied. The twist angle accuracy is typically $\pm 0.5^\circ$. All of the samples are encapsulated between hexagonal boron nitride (hBN) substrates to prevent environmental degradation. The structure and twist angle of a small number of samples were verified by scanning transmission electron microscopy (STEM). These samples are difficult to fabricate; they are encapsulated by very thin hBN layers (< 5 nm) and deposited on 8-nm-thick amorphous SiO₂ membranes to achieve good detection sensitivity (Extended Data Fig. 2). We have also fabricated a number of dual-gated field-effect devices, which allow us to continuously tune the interlayer AF exchange interaction in the M-regions by varying the doping level in CrI₃ (Ref. ^{26, 27}). (See Methods for details on device fabrication and characterizations.)

Figure 1c shows the electron diffraction pattern of a sample with a target twist angle of $\theta = 1.5^\circ$. Diffraction spots from both hBN and CrI₃ are observed. The third-order diffraction spots from twisted CrI₃ (circled) correspond to a Fourier-transformed distance of $a/3 = 0.23$ nm (a is the in-plane lattice constant of CrI₃). Because of the finite twist angle, each CrI₃ diffraction spot consists of a pair of shifted diffraction spots, producing a slightly elongated spot. Figure 1d-1f show the dark-field images, each constructed from a single circled diffraction spot in Fig. 1c. A clear moiré stripe pattern with periodicity one third of the moiré period $a_M/3 = 6.1 \pm 0.9$ nm is seen. Each image is related to the other by a 60° rotation. The real-space moiré pattern can be constructed by superimposing the three images (Extended Data Figure 2). Using the measured $a_M = 18.3 \pm 2.7$ nm, we determine the twist angle to be $\theta = 2 \sin^{-1} \left(\frac{a}{2a_M} \right) \approx 2.2 \pm 0.3^\circ$. The STEM measurement of another sample (Extended Data Fig. 3) shows a twist angle of $2.5 \pm 0.5^\circ$ for a target of 2° . These results verify the formation of moiré structures in twisted bilayer CrI₃ and the twist angle accuracy in the fabrication process.

We probe the magnetic ground state of twisted bilayer samples of CrI₃ by magnetic circular dichroism (MCD) measurements. Under our experimental conditions the MCD is linearly proportional to the out-of-plane component of the magnetization. However, a direct comparison of the absolute MCD for different samples is not appropriate because of the different local field factors from different substrate thicknesses. Unless otherwise specified, all measurements are performed at 4 K.

Figure 2a-2d show the MCD as a function of out-of-plane magnetic field B for four bilayer samples. Extended Data Fig. 5, 6 show results for additional samples, and Extended Data Fig. 2 and 3, the correlated STEM and MCD studies. A natural bilayer with M-stacking (Fig. 2a) is included as a reference. Its MCD is negligible till the field reaches the critical value $B_c \approx 0.6$ T for the spin-flip transition; the behavior is fully consistent with the A-type AF state reported in the literature^{2, 28}. Also included is the MCD from an isolated monolayer (Fig. 2b, red line); it shows the expected FM loop. The magnetic response is diametrically different in the 1.2°-twist sample (Fig. 2b). Both AF-like and FM-like behaviors are present. In addition to the spin-flip transition near $B_c \approx 0.5 - 0.6$ T, a FM loop centered at zero field emerges. The result shows the coexistence of the AF and FM domains.

With increasing twist angle θ , the AF contribution quickly diminishes: a very small AF contribution remains in the 4°-twist sample; only the FM contribution is observed in the 15°-twist sample. We denote the fraction of the FM and AF domains in the sample by $f_{FM} \approx \frac{MCD(0 T)}{MCD(1 T)}$ and $f_{AF} \approx 1 - f_{FM}$, respectively. (We have ignored the domain walls; they are estimated in Methods to be narrow compared to the moiré period at low temperatures). The twist angle dependence of f_{FM} is summarized in Fig. 3 (top panel). The AF-FM coexistence disappears at a critical angle $\theta_c \sim 3^\circ$, above which only FM is observed. Below θ_c the spin-flip transition field B_c is weakly angle dependent (lower panel). On the other hand, the FM coercive field does not vary significantly in all twisted bilayer and monolayer samples.

We characterize the spatial homogeneity of the magnetic properties of twisted bilayers by MCD imaging. Figure 2e and 2f show $[MCD(1 T) - MCD(0 T)]$ and $MCD(0 T)$, respectively, which represent the AF and FM contributions in the 1.2°-twist sample (the boundary of each CrI₃ monolayer is marked by dashed curves). We observe $f_{AF} \approx 0$ in the isolated monolayer regions as expected, and a finite f_{AF} in most twisted bilayer regions. The FM contribution in the bilayer regions is comparable to that of the isolated monolayers. The result shows homogeneous AF-FM coexistence. On the other hand, in twisted bilayers with $\theta > \theta_c$ the AF contribution is absent over the entire sample (Extended Data Fig. 6), and the FM signal nearly doubles that of the isolated monolayer regions (Fig. 2g for $\theta = 4^\circ$, Fig. 2h for $\theta = 15^\circ$).

We further examine the temperature dependence of the magnetic response of the 1.2°-twist sample in Fig. 4. Figure 4b shows the magnetic-field dependence of the MCD at varying temperatures. The FM and AF fractions (f_{FM} and f_{AF}) are nearly temperature independent for the entire temperature range. More details are displayed in Fig. 4a, which

is a contour of the MCD as a function of temperature and field scanned from -1.5 T to 1.5 T. Upon cooling, the coercive field of the FM contribution increases monotonically. This is consistent with the behavior of monolayer CrI₃. The spin-flip transition field B_c first increases and then decreases slightly when the temperature further decreases. This deviates from the monotonic increase of B_c upon cooling in natural bilayer CrI₃ (Extended Data Fig. 7). The temperature dependences of the FM coercive field and the spin-flip transition field are summarized in Fig. 4c. For samples with $\theta > \theta_c$ we measure the temperature dependence of the magnetic AC susceptibility, which shows a single diverging peak, indicating a fully coupled bilayer, and a Curie temperature substantially higher than the monolayers (Extended Data Fig. 4).

The distinct behavior of twisted bilayers and FM monolayers, including the presence of AF contributions for $\theta < \theta_c$ and higher Curie temperatures for $\theta > \theta_c$, is a manifestation of the interlayer magnetic interactions in twisted bilayers. The observed nearly constant coercive field does not contradict it because the coercive field is mainly determined by the intralayer magnetic anisotropy and sample temperature. The observed AF-FM coexistence in small-twist-angle CrI₃ bilayers shows the formation of AF and FM domains; the domain size is substantially smaller than the diffraction limited laser spot size of ~ 500 nm since the MCD images are highly homogeneous. Furthermore, consistent behavior observed in multiple samples of similar twist angle suggests that external origins such as strain are unlikely.

Our results are consistent with the emergence of a noncollinear magnetic ground state driven by competing magnetic interactions in a moiré superlattice¹⁰. The moiré superlattice of twisted bilayer CrI₃ contains spatially modulated M- and R-stacking structures (Fig. 1a), which support the AF and FM interlayer exchange coupling, respectively. Because the interlayer FM exchange in the R-phase is substantially stronger than the interlayer AF exchange in the M-phase²⁰, we only need to consider the competition between the formation of the AF domains and the AF-FM domain walls. The energy gain per moiré unit cell from forming the AF domains in the M-regions, $\sim 2f_{AF} \left(\frac{a_M}{a}\right)^2 J_{\perp}$, scales with the area of the moiré unit cell. The energy cost per moiré unit cell from forming the AF-FM domain walls near the M-R stacking boundaries, $\sim \pi \left(\frac{a_M}{a}\right) \sqrt{J_{\parallel}(K + 2J_{\perp})}$, scales with the period of the moiré unit cell (Methods). Here $J_{\perp} \sim 0.1$ meV is the interlayer AF exchange constant^{2,28}, $J_{\parallel} \sim 2$ meV is the intralayer FM exchange constant²⁹, and $K \sim 0.3$ meV is the single-ion magnetic anisotropy energy in CrI₃ (Ref.³⁰). The different scaling of the two energy terms with moiré period guarantees that at small twist angle (or large a_M) the energy gain from forming the AF domains wins and a noncollinear magnetic ground state with spatially modulated AF and FM regions emerges (Fig. 1b). The critical twist angle can be estimated by equating the two energy terms to yield $\theta_c \sim \frac{f_{AF} J_{\perp}}{\sqrt{J_{\parallel}(K+2J_{\perp})}} \approx 3^\circ$. The value is in good agreement with experiment. In addition, below $\theta \sim 2^\circ$, experiment shows saturation of f_{FM} to ~ 0.6 (Fig. 3). Large-scale structural relaxation at small twist angles is therefore unlikely since the R-stacking is the most stable structure (Ref.^{15,16,20}) and would favor $f_{FM} \approx 1$.

Above the critical angle, a collinear FM ground state is preferred. The transition from a noncollinear to a collinear magnetic state can be continuous (for small K/J_{\perp}) or abrupt (for large K/J_{\perp}) (Ref. ¹⁰). In the continuous phase transition scenario, an intermediate noncollinear state with spins flop to the in-plane direction in the AF or FM domains is further expected. In CrI₃ with large magnetic anisotropy ($K/J_{\perp} \sim 3$), the intermediate state has a high energy cost and an abrupt transition is favored. This is consistent with experiment, in which spin-flip transitions are observed in all small-twist-angle bilayers. Because of the large magnetic anisotropy, the domain wall width is small compared to a_M (Methods) so that B_c is weakly angle dependent for $\theta < \theta_c$ (Fig. 3).

The non-monotonic temperature dependence of B_c is also a manifestation of the competing AF and FM interactions. In natural bilayer CrI₃ with M-stacking, the spin-flip transition occurs at $B_c \sim \frac{2J_{\perp}}{3\mu_B}$ (Ref. ²⁸), at which the Zeeman energy gain $3\mu_B B$ of the FM state overcomes the interlayer AF exchange energy cost $2J_{\perp}$. Here μ_B is the Bohr magneton and each Cr ion carries $3\mu_B$. In twisted bilayer CrI₃, the presence of AF and FM domains lowers the energy cost for the spin-flip transition by the domain wall energy

and gives $B_c \sim \frac{2f_{AF}J_{\perp} - \pi\left(\frac{\alpha}{a_M}\right)\sqrt{J_{\parallel}(K+2J_{\perp})}}{f_{AF}(3\mu_B)}$ (Methods). The exchange constants $J_{\parallel}, J_{\perp} \propto t^{\alpha}$

(with $\alpha < 1$) and the anisotropy energy $K \propto t^{\beta}$ (with $\beta > 1$) have distinct scaling dependences on the reduced temperature $t = \frac{T_c - T}{T_c}$ (T_c is the critical temperature) ³¹⁻³³.

Using $\alpha = 0.22$ (Ref. ²⁹) for both J_{\parallel} and J_{\perp} and $\beta = 2.3$, we can reproduce the observed non-monotonic temperature dependence of B_c in Fig. 4c (red line).

Finally, we demonstrate gate control of the noncollinear magnetic state and further verify its origin from competing interlayer exchange interactions. Figure 5a shows the magnetic-field dependence of MCD (normalized by the saturated value at 1 T) at varying gate voltages for the 1.2°-twist sample. With increasing gate voltage (corresponding to electron doping), the spin-flip transition field B_c decreases by as much as $\sim 50\%$ while the FM loop is little affected. The result shows that the primary effect of electron doping is to weaken the interlayer AF exchange J_{\perp} in the M-regions. This is consistent with earlier reports on natural bilayer CrI₃ (Ref. ^{26, 27}). Meanwhile, the remnant magnetization as manifested by $MCD(0 T) \propto f_{FM}$ increases by $\sim 10\%$ with gating (Fig. 5b). (Extended Data Fig. 8 shows similar result from another device.) Such an increase reflects shrinkage of the AF domains (or equivalently, expansion of the FM domains) as the interlayer AF exchange constant J_{\perp} is weakened. At sufficiently high electron doping densities, where J_{\perp} becomes smaller than the critical value $J_{\perp c} \sim \theta\sqrt{J_{\parallel}K}/f_{AF}$ (Methods), the energy gain from forming AF domains in the M-regions would become smaller than the energy cost of forming AF-FM domain walls, and an abrupt quantum phase transition from a noncollinear state to a collinear FM state is expected ¹⁰. Tuning J_{\perp} by electron doping in a sample with fixed twist angle θ is therefore similar to varying θ while keeping J_{\perp} constant (Fig. 3). Future studies with higher electron doping densities will provide a promising route to achieve a gate-voltage-induced magnetic quantum phase transition.

In conclusion, we have realized moiré superlattices of 2D magnetic crystals and demonstrated a new noncollinear magnetic ground state in small-twist-angle bilayer CrI_3 , which can be further tuned by either twist angle or electrical gating. Our results support the formation of AF and FM domains from competing interlayer exchange interactions in moiré superlattices and are consistent with the predictions of a spin model for twisted bilayer magnetic materials¹⁰⁻¹⁴. High-resolution and high-sensitivity magnetic characterizations are warranted for imaging of the new magnetic states in future studies. Our study forms the basis for engineering moiré magnetism in twisted bilayer magnetic crystals and high-density gate-voltage-controlled magnetic devices for applications.

Methods

Device fabrication

We fabricated twisted bilayer CrI_3 devices by the “tear-and-stack” method²³⁻²⁵ inside a glove box with water and oxygen levels below 1 part per million (ppm). Monolayer CrI_3 was mechanically exfoliated from bulk CrI_3 crystals onto SiO_2/Si substrates and identified by its optical contrast under a microscope. One example is shown in Extended Data Fig. 1a. We picked up a part of the flake (the black dashed curve) from the substrate with a polydimethylsiloxane/polycarbonate (PDMS/PC) stamp and then twisted the remaining part (the red dashed curve in Extended Data Fig. 1b) on the substrate by an angle θ that ranges from 0° to 60° . A fine angle control is achieved by using a high-precision rotation stage (Thorlabs PR01). Finally, we engaged the two monolayers to form a twisted bilayer (Extended Data Fig. 1c). The finished twisted bilayer was encapsulated by hBN and contacted with graphene electrodes. A subset of the samples also has extra few-layer graphene as top and bottom gate electrodes. We also fabricated a small number of hBN-encapsulated samples and transferred onto TEM windows made of 8-nm-thick amorphous SiO_2 membranes for the STEM studies. Thinner hBN substrates (with thickness less than 5 nm) are used to reduce the hBN diffraction intensity. All of the encapsulated samples are chemically stable. Measurements over multiple cycles can be performed without any sign of sample degradation.

MCD measurements

Similar MCD measurements on 2D CrI_3 have been reported in earlier studies^{15, 26, 28}. In short, an incident He-Ne laser beam (633 nm) was focused onto the sample plane to a diffraction-limited spot (~ 500 nm in diameter) under normal incidence using a microscope objective of high numerical aperture (N.A. ~ 0.81). The polarization of the incident light was modulated between left and right circular polarization by a photoelastic modulator. The reflected light was collected by the same objective and directed to a biased photodiode. The AC and DC components of the reflected light were collected by a lock-in amplifier and a multi-meter, respectively. The MCD signal is defined as the ratio of the AC to the DC signal. For MCD imaging studies, we used a filtered tungsten halogen lamp output (centered at 633 nm with a bandwidth ~ 10 nm) for broad-field illumination in the same setup. The reflected light intensity from left- and right-handed illumination was collected to a charge-coupled device (CCD) that produces an optical image of the sample. The MCD image at a given magnetic field is obtained by normalizing the difference between the two images by their sum.

4D-STEM imaging and image analysis

The twisted bilayer CrI₃ sample was imaged in an FEI F20 S/TEM at 200 kV using a 10 μm condenser aperture and a probe semi-convergence angle of ~ 1.5 mrad. The sample was imaged using the 4D-STEM technique, in which an electron probe is stepped over a scan region and a full electron diffraction pattern is recorded at each pixel step. The final 4D dataset (2D diffraction pattern \times 2D image) was then used to recover details about the local crystal structure over large fields of view. All 4D-STEM imaging was done using the Electron Microscope Pixel Array Detector (EMPAD)³⁴. The high dynamic range of the EMPAD ($10^6:1$) allows for the collection of both the direct and scattered electron beams. A real-space scan size of 256×256 pixels and an acquisition time of 3 ms/pixel were used.

The 4D-STEM data were screened and processed using the Cornell Spectrum Imager³⁵. Each 4D-STEM dataset consists of a 2D real-space scan and a 2D diffraction pattern associated with each real-space pixel in that scan. Virtual dark field images are created by masking a region of the diffraction pattern and summing over the contributions of each pixel in the mask to obtain the intensity of the real-space image. The average moiré periodicity was calculated from the fast Fourier transform (FFT) of one of the dark field images. The FFT contains a pair of peaks arising from the real-space moiré. A line profile was taken through the FFT and Gaussian functions were fitted to the peaks in MATLAB. The moiré periodicity and uncertainty were taken to be the mean and one standard deviation from the Gaussian fit parameters. Using this method, the moiré period in Figure 1d-1f was found to be 18.3 ± 2.7 nm.

AF-FM domain wall width

We consider a model that involves an abrupt physical boundary between the monoclinic and rhombohedral stacking regions in the moiré superlattice of twisted bilayer CrI₃. The simple model is intended to provide an order of magnitude estimate of the experimental observations. Since the interlayer FM exchange interaction for rhombohedral stacking is predicted to be substantially stronger than the interlayer AF exchange interaction for monoclinic stacking²⁰, we assume the AF-FM domain walls can only form in the monoclinic stacking regions. The domain wall energy per moiré unit cell consists of three terms:

$$E_{DW} \sim \pi^2 \left(\frac{a_M}{\delta} \right) \frac{J_{\parallel}}{2} + \left(\frac{\delta a_M}{2a^2} \right) (K + 2J_{\perp}). \quad (1)$$

Here δ is the domain wall width and $\frac{\delta a_M}{a^2} \sim N$ is the number of spins in the domain wall (per moiré unit cell). The first two terms, involving intralayer FM exchange J_{\parallel} and magnetic anisotropy K , constitute the standard expression for the energy cost of forming domain walls in FM materials. They compete against each other; a larger J_{\parallel} favors a wider domain wall; conversely, a larger K favors a narrower domain wall. The last term is the energy cost from interlayer exchange interactions in the monoclinic stacking regions. It can be evaluated from $\sum_{i=1}^N J_{\perp} (1 + \cos \phi_i) \approx \frac{NJ_{\perp}}{\pi} \int_0^{\pi} d\phi (1 + \cos \phi)$, where ϕ

is the angle between the top and bottom layer spins. Minimizing E_{DW} with respect to δ yields an expression for the domain wall width

$$\delta \sim \pi \sqrt{\frac{J_{\parallel} a^2}{K + 2J_{\perp}}}. \quad (2)$$

It is analogous to the result for domain walls in FM materials, $\delta \sim \pi \sqrt{\frac{J_{\parallel} a^2}{K}}$, with the modification of $K \rightarrow K + 2J_{\perp}$. We estimate the domain wall width in CrI_3 to be about 4 nm at low temperatures, which is substantially smaller than $a_M \sim 20$ nm. At higher temperatures (still below T_C), where the magnetic anisotropy energy K becomes negligible compared to J_{\perp} , the domain wall width becomes $\delta \sim \pi \sqrt{\frac{J_{\parallel} a^2}{2J_{\perp}}}$. Therefore, δ here is expected to have a much weaker temperature dependence compared to that in the FM materials.

Critical twist angle and interlayer exchange coupling

In the above model, the noncollinear magnetic ground state is originated from the competing magnetic interactions between the formation of the AF-FM domain walls and the interlayer AF exchange in the monoclinic stacking regions. A noncollinear state is favored only if the latter dominates. The energy gain per moiré unit cell from having AF domains in the monoclinic stacking regions is:

$$E_{AF} \sim 2f_{AF} \left(\frac{a_M}{a}\right)^2 J_{\perp}. \quad (3)$$

The energy cost per moiré unit cell from forming the domain walls, after substituting (2) into (1), is:

$$E_{DW} \sim \pi \left(\frac{a_M}{a}\right) \sqrt{J_{\parallel}(K + 2J_{\perp})}. \quad (4)$$

The noncollinear-to-collinear phase transition occurs when $E_{AF} \sim E_{DW}$. If the transition is tuned by the twist angle θ , we can obtain a critical angle, by using $\frac{a}{a_M} = 2 \sin \frac{\theta}{2} \approx \theta$,

$$\theta_c \sim \frac{f_{AF} J_{\perp}}{\sqrt{J_{\parallel}(K + 2J_{\perp})}}. \quad (5)$$

Alternatively, if the transition is tuned by varying J_{\perp} through gating at a fixed twist angle θ , we can obtain a critical interlayer exchange, by keeping the leading order term,

$$J_{\perp c} \sim \theta \sqrt{J_{\parallel} K} / f_{AF}. \quad (6)$$

Spin-flip transition field

The spin-flip transition field B_C for the AF domains in the noncollinear phase can be evaluated following similar consideration of the energetics. The application of an external

magnetic field favors the collinear state. The magnetic energy per moiré unit cell of the monoclinic stacking regions for the collinear state is

$$E_{col} \sim f_{AF} \left(\frac{a_M}{a} \right)^2 (J_{\perp} - 3\mu_B B). \quad (7)$$

The first term is the energy cost for having an interlayer FM configuration in the collinear state; and the second term is the Zeeman energy gain for the FM state. On the other hand, the energy per moiré unit cell at the monoclinic stacking regions for the noncollinear state is

$$E_{ncol} \sim E_{DW} - f_{AF} \left(\frac{a_M}{a} \right)^2 J_{\perp}. \quad (8)$$

The first term is the energy cost for forming domain walls and the second term is the energy gain for having an interlayer AF configuration in the monoclinic stacking regions. The spin-flip transition field can be obtained by equating (7) and (8):

$$B_c \sim \frac{2f_{AF}J_{\perp} - \pi \left(\frac{a}{a_M} \right) \sqrt{J_{\parallel}(K+2J_{\perp})}}{f_{AF}(3\mu_B)}. \quad (9)$$

References:

1. Gong, C. et al. Discovery of intrinsic ferromagnetism in two-dimensional van der Waals crystals. *Nature* **546**, 265-269 (2017).
2. Huang, B. et al. Layer-dependent ferromagnetism in a van der Waals crystal down to the monolayer limit. *Nature* **546**, 270-273 (2017).
3. Burch, K.S., Mandrus, D. & Park, J.-G. Magnetism in two-dimensional van der Waals materials. *Nature* **563**, 47-52 (2018).
4. Gong, C. & Zhang, X. Two-dimensional magnetic crystals and emergent heterostructure devices. *Science* **363**, eaav4450 (2019).
5. Mak, K.F., Shan, J. & Ralph, D.C. Probing and controlling magnetic states in 2D layered magnetic materials. *Nature Reviews Physics* **1**, 646-661 (2019).
6. Gibertini, M., Koperski, M., Morpurgo, A.F. & Novoselov, K.S. Magnetic 2D materials and heterostructures. *Nature Nanotechnology* **14**, 408-419 (2019).
7. Andrei, E.Y. & MacDonald, A.H. Graphene bilayers with a twist. *Nature Materials* **19**, 1265-1275 (2020).
8. Balents, L., Dean, C.R., Efetov, D.K. & Young, A.F. Superconductivity and strong correlations in moiré flat bands. *Nature Physics* **16**, 725-733 (2020).
9. Kennes, D.M. et al. Moiré heterostructures as a condensed-matter quantum simulator. *Nature Physics* **17**, 155-163 (2021).
10. Hejazi, K., Luo, Z.-X. & Balents, L. Noncollinear phases in moiré magnets. *Proceedings of the National Academy of Sciences* **117**, 10721 (2020).
11. Tong, Q., Liu, F., Xiao, J. & Yao, W. Skyrmions in the Moiré of van der Waals 2D Magnets. *Nano Letters* **18**, 7194-7199 (2018).
12. Akram, M. & Erten, O. Skyrmions in twisted van der Waals magnets. *Physical Review B* **103**, L140406 (2021).

13. Xiao, F., Chen, K. & Tong, Q. Magnetization textures in twisted bilayer CrX₃ (X=Br, I). *Physical Review Research* **3**, 013027 (2021).
14. Wang, C., Gao, Y., Lv, H., Xu, X. & Xiao, D. Stacking Domain Wall Magnons in Twisted van der Waals Magnets. *Physical Review Letters* **125**, 247201 (2020).
15. Li, T. et al. Pressure-controlled interlayer magnetism in atomically thin CrI₃. *Nature Materials* **18**, 1303-1308 (2019).
16. Song, T. et al. Switching 2D magnetic states via pressure tuning of layer stacking. *Nature Materials* **18**, 1298-1302 (2019).
17. Andrei, E.Y. et al. The marvels of moiré materials. *Nature Reviews Materials* **6**, 201-206 (2021).
18. Chen, W. et al. Direct observation of van der Waals stacking-dependent interlayer magnetism. *Science* **366**, 983 (2019).
19. Klein, D.R. et al. Enhancement of interlayer exchange in an ultrathin two-dimensional magnet. *Nature Physics* **15**, 1255-1260 (2019).
20. Sivadas, N., Okamoto, S., Xu, X., Fennie, C.J. & Xiao, D. Stacking-Dependent Magnetism in Bilayer CrI₃. *Nano Letters* **18**, 7658-7664 (2018).
21. Li, S. et al. Magnetic-Field-Induced Quantum Phase Transitions in a van der Waals Magnet. *Physical Review X* **10**, 011075 (2020).
22. Yoo, H. et al. Atomic and electronic reconstruction at the van der Waals interface in twisted bilayer graphene. *Nature Materials* **18**, 448-453 (2019).
23. Kim, K. et al. van der Waals Heterostructures with High Accuracy Rotational Alignment. *Nano Letters* **16**, 1989-1995 (2016).
24. Cao, Y. et al. Superlattice-Induced Insulating States and Valley-Protected Orbits in Twisted Bilayer Graphene. *Physical Review Letters* **117**, 116804 (2016).
25. Chung, T.-F., Xu, Y. & Chen, Y.P. Transport measurements in twisted bilayer graphene: Electron-phonon coupling and Landau level crossing. *Physical Review B* **98**, 035425 (2018).
26. Jiang, S., Li, L., Wang, Z., Mak, K.F. & Shan, J. Controlling magnetism in 2D CrI₃ by electrostatic doping. *Nature Nanotechnology* **13**, 549-553 (2018).
27. Huang, B. et al. Electrical control of 2D magnetism in bilayer CrI₃. *Nature Nanotechnology* **13**, 544-548 (2018).
28. Jiang, S., Shan, J. & Mak, K.F. Electric-field switching of two-dimensional van der Waals magnets. *Nature Materials* **17**, 406-410 (2018).
29. Chen, L. et al. Topological Spin Excitations in Honeycomb Ferromagnet CrI₃. *Physical Review X* **8**, 041028 (2018).
30. McGuire, M.A., Dixit, H., Cooper, V.R. & Sales, B.C. Coupling of Crystal Structure and Magnetism in the Layered, Ferromagnetic Insulator CrI₃. *Chemistry of Materials* **27**, 612-620 (2015).
31. Blundell, S. *Magnetism in Condensed Matter*. (Oxford Univ. Press, Oxford, 2001).
32. Zener, C. Classical Theory of the Temperature Dependence of Magnetic Anisotropy Energy. *Physical Review* **96**, 1335-1337 (1954).
33. Niitsu, K., Tanigaki, T., Harada, K. & Shindo, D. Temperature dependence of 180° domain wall width in iron and nickel films analyzed using electron holography. *Applied Physics Letters* **113**, 222407 (2018).

34. Tate, M.W. et al. High Dynamic Range Pixel Array Detector for Scanning Transmission Electron Microscopy. *Microscopy and Microanalysis* **22**, 237-249 (2016).
35. Cueva, P., Hovden, R., Mundy, J.A., Xin, H.L. & Muller, D.A. Data Processing for Atomic Resolution Electron Energy Loss Spectroscopy. *Microscopy and Microanalysis* **18**, 667-675 (2012).

Figures and figure captions

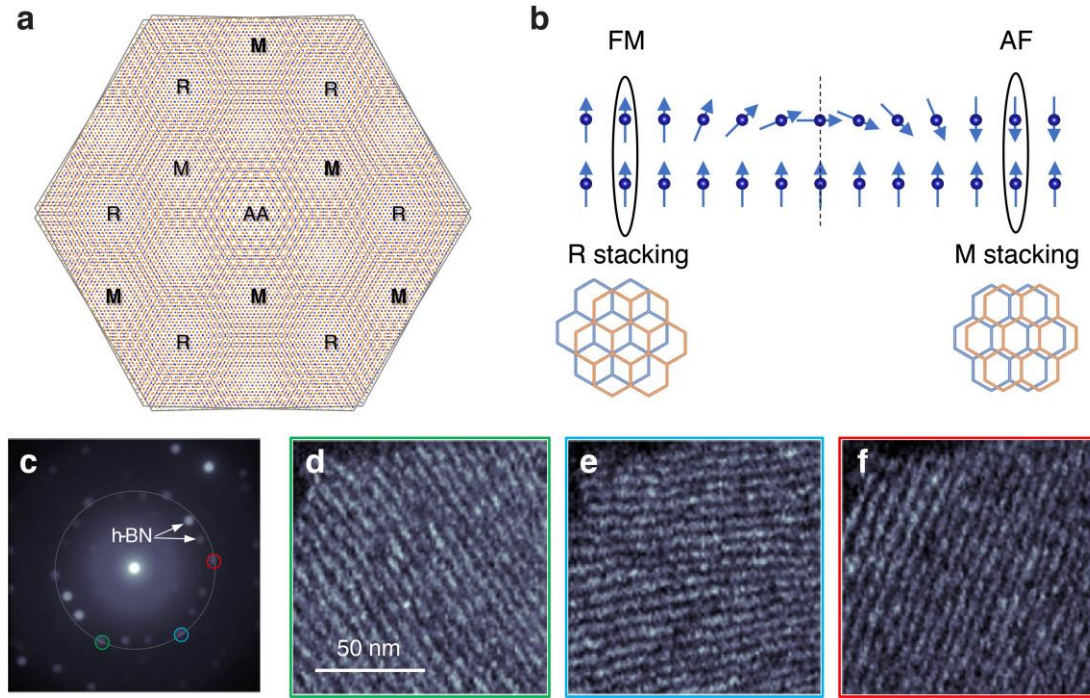


Figure 1 | Moiré superlattice structure of twisted bilayer CrI₃. **a**, Moiré superlattice structure of twisted bilayer CrI₃ with a small twist angle θ . R, M and AA denote rhombodromal, monoclinic and AA stacking, respectively. The R and M stacking are shown in **b** with blue and orange denoting two adjacent CrI₃ monolayers. **b**, Schematic illustration of a magnetic domain wall formed between the R- and M-stacking regions. Balls and arrows denote the spins of magnetic ions. **c**, Electron-beam diffraction pattern from a small-angle twisted bilayer CrI₃ sample, down the $\langle 001 \rangle$ zone axis (perpendicular to sample surface). The two arrows indicate the diffraction spots (six pairs in total) from the top and bottom hBN capping layers. The big dashed circle tracks the $\langle 300 \rangle$ diffraction spots for CrI₃. The spots circled in green, blue and red are the dark field masks for the real-space dark field moiré fringe patterns in **d-f**, respectively. The scale bar is 50 nm.

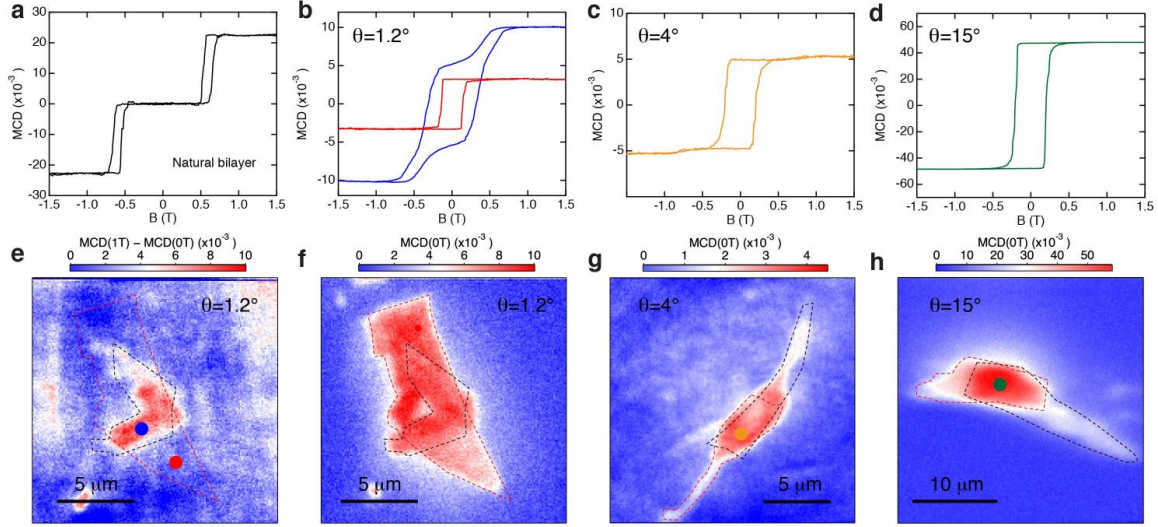


Figure 2 | MCD microscopy of twisted bilayer CrI_3 . **a-d**, Magnetic-field dependence of MCD of a natural bilayer CrI_3 (**a**) and twisted bilayer CrI_3 with twist angle 1.2° (**b**), 4° (**c**) and 15° (**d**). The MCD signal of an isolated monolayer CrI_3 is shown in **b** for comparison (red). Coexistence of AF and FM contributions is evident at small twist angles. **e**, Image of $MCD(1T) - MCD(0T)$ for the 1.2° sample, illustrating the AF fraction of the sample. Non-zero contrast is observed only in the twisted bilayer region. **f-h**, MCD images at $B = 0$ T for the 1.2° (**f**), 4° (**g**) and 15° (**h**) samples (samples are polarized at 1 T prior to the MCD measurement). They show the FM fraction of the samples. In all images the dashed black and red lines outline the constituent monolayer regions. The colored dots denote the locations of the MCD measurements of the same color in **b-d**.

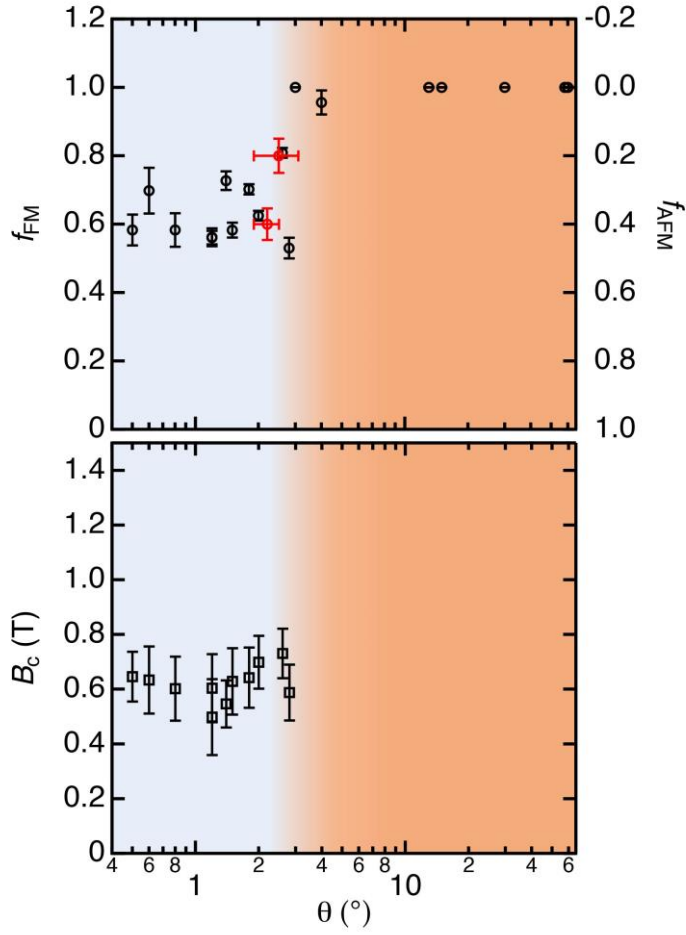


Figure 3 | Twist angle dependence. Upper panel: the FM and AF fraction, f_{FM} (left axis) and f_{AF} (right axis), as a function of target twist angle θ for all measured samples. The vertical error bars are estimated from measurements at different sample locations and indicate the spatial inhomogeneity. The twist angle uncertainty is estimated to be about 0.5° (not shown); it is characterized for two samples (red circle) by the STEM and shown. At small twist angles ($\theta \lesssim 3^\circ$), $f_{\text{FM}} < 1$ indicates a mixed AF-FM ground state; a pure FM ground state is observed at $\theta \gtrsim 4^\circ$. Lower panel: twist angle dependence of the spin-flip transition field B_c . The vertical error bars are estimated from the field span of the spin-flip transition²⁸.

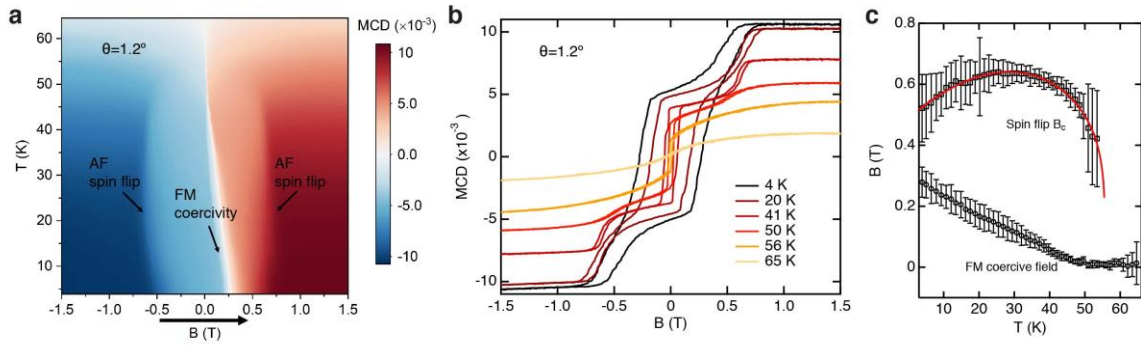


Figure 4 | Temperature dependence. **a**, MCD as a function of temperature and magnetic field (sweeping from negative to positive) for a 1.2° -twist bilayer CrI_3 . **b**, Magnetic-field dependence of the MCD (for both forward and backward sweeps) at representative temperatures for the same sample. **c**, The extracted spin-flip transition field B_c (top) and the FM coercive field (bottom) as function of temperature. B_c is the average spin-flip transition field between forward and backward sweeps. The red curve is a fit to B_c using the model described in the main text. The vertical error bars are estimated from the field span of the magnetic transitions.

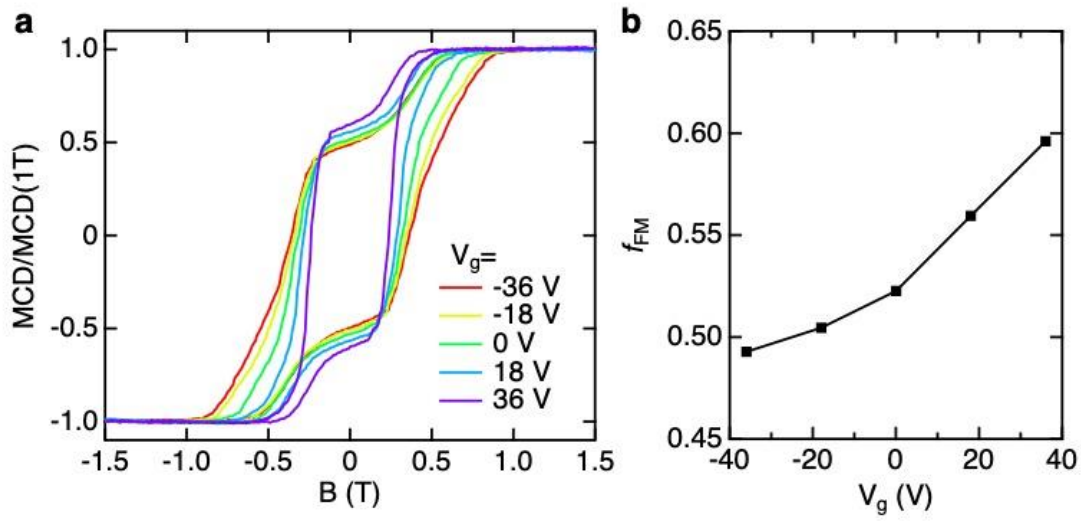
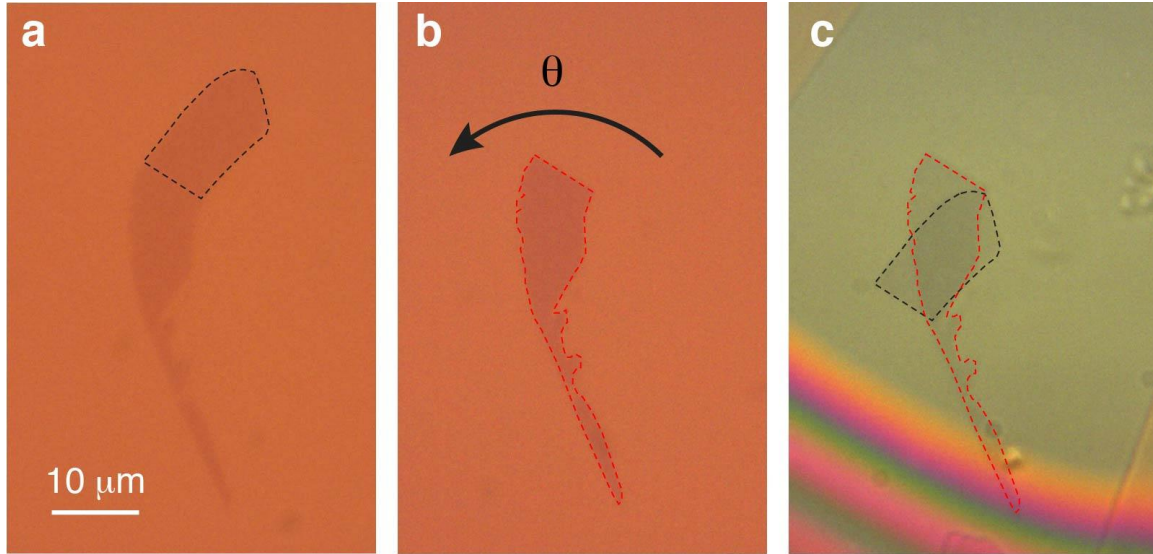
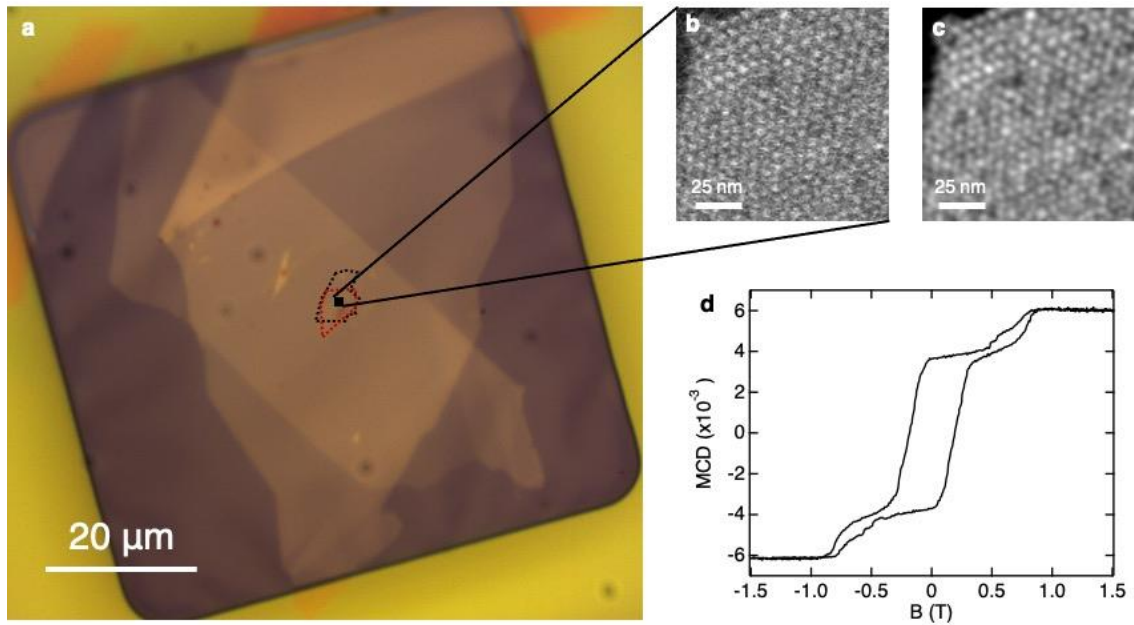


Figure 5 | Gate control of the noncollinear magnetic state. **a**, MCD (normalized to 1 at large fields) as a function of magnetic field at selected gate voltages (V_g). V_g is the total gate voltage applied symmetrically to the top and bottom gates. **b**, FM fraction f_{FM} as a function of V_g .

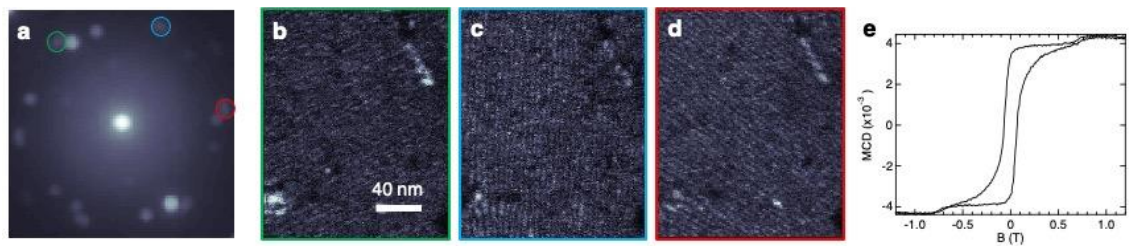
Extended Data Figures



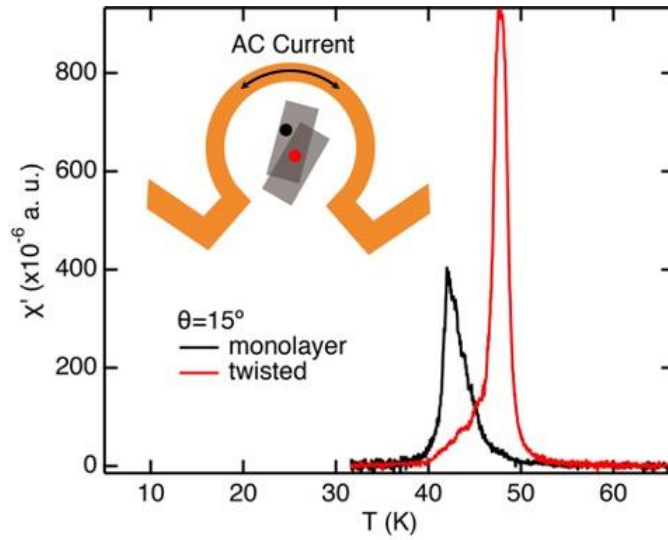
Extended Data Figure 1 | “Tear-and-stack” method. a-c, Optical images taken during the preparation of a twisted bilayer CrI₃ sample. The monolayer in **a** is torn apart partially (outlined by the black dashed curves) and picked up by an hBN flake, leaving the remaining portion on the substrate. The remaining portion in **b** (outlined by the red dashed curves) is rotated by an angle θ . The two monolayers of CrI₃ are finally engaged to form a twisted bilayer (**c**). The scale bar is 10 micrometers.



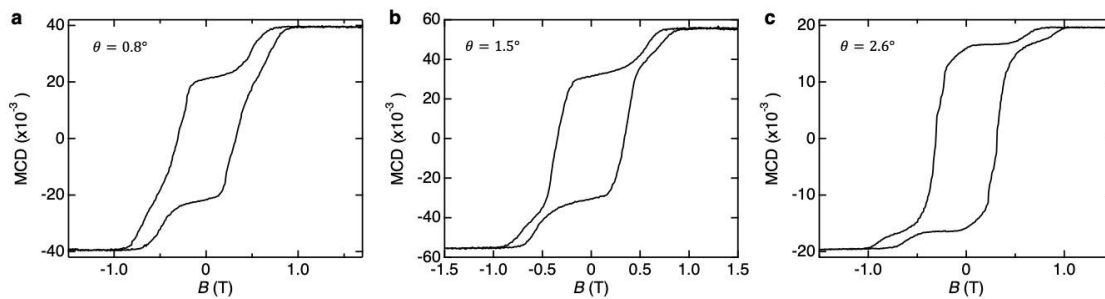
Extended Data Figure 2 | Correlated STEM and MCD studies (sample 1). **a**, Optical image of the sample for the STEM measurements shown in Fig. 1. The scale bar is 20 micrometers. **b,c**, Sum of the STEM dark field images in Fig. 1d-1f before (**b**) and after (**c**) applying a $\sigma=1.25$ pixel Gaussian filter. Since the image is constructed from the third-order diffraction spots from twisted CrI_3 , the true moiré period is three times the value shown in this figure. The scale bars are 25 nm. **d**, MCD measurement performed on the same sample area. No significant changes were observed in the MCD before and after the STEM measurements.



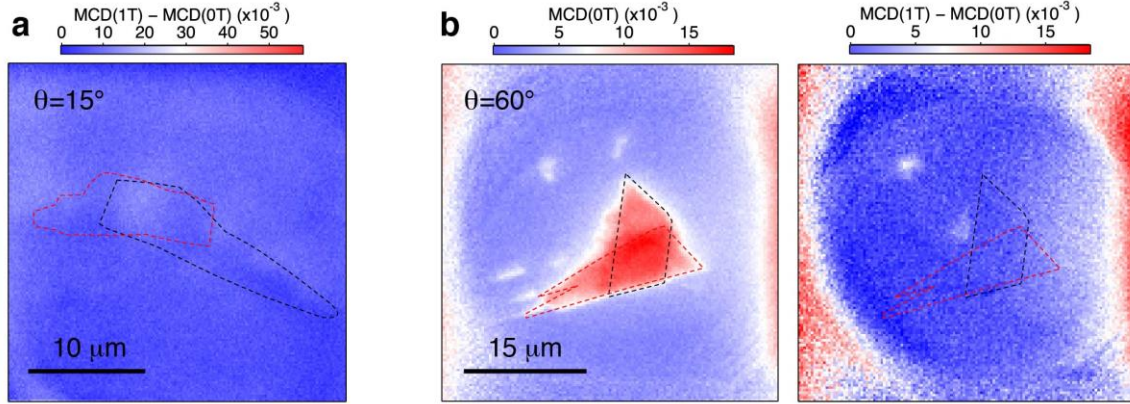
Extended Data Figure 3 | Correlated STEM and MCD studies (sample 2). **a-d**, Electron diffraction and the corresponding real-space dark field moiré fringe patterns for sample 2, with the twist angle estimated to be $2.5 \pm 0.5^\circ$. The target twist angle is 2° . **e**, MCD measurement performed on the same sample area.



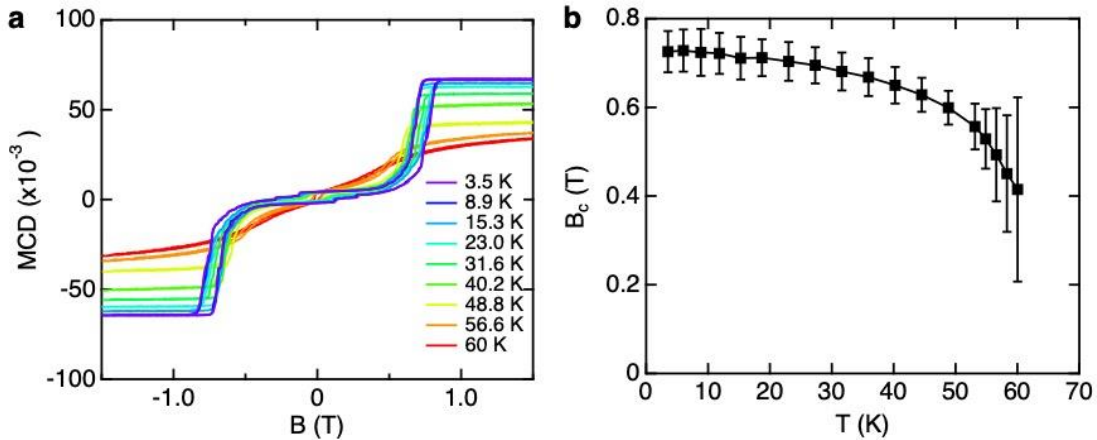
Extended Data Figure 4 | Temperature dependent AC susceptibility (15°-twist sample). The inset shows the sample and the AC susceptibility measurement schematic. An AC current through the metallic ring structure is used to generate a small oscillating magnetic field of a few Oe. The AC susceptibility is measured using MCD as $\chi' = \frac{\partial MCD}{\partial H}$ (details of the method are described in ref. ²⁶). The twisted bilayer region (red) shows a single divergent peak of $\chi'(T)$, indicating FM coupling of the two layers and the absence of uncoupled regions. The Curie temperature is ~ 6 K higher in the twist bilayer than in the isolated monolayer region (black).



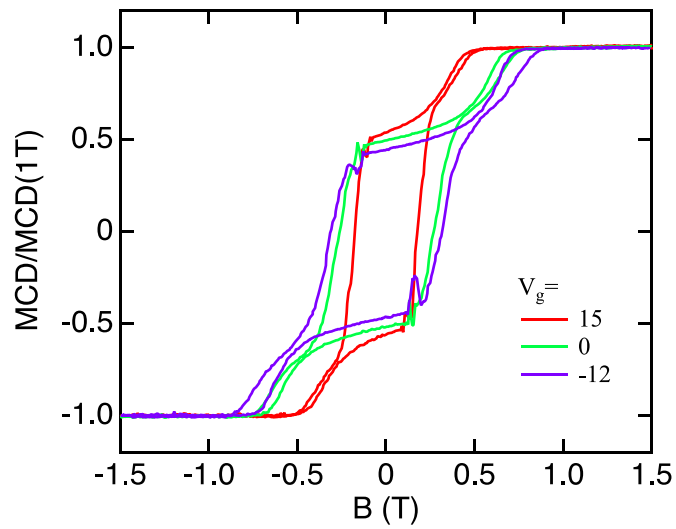
Extended Data Figure 5 | Additional MCD data at 4 K for samples with twist angles 0.8° (a), 1.5° (b) and 2.6° (c).



Extended Data Figure 6 | Additional MCD imaging data. **a**, Map of $MCD(1T) - MCD(0T)$ for 15° -twist bilayer CrI_3 . No AF contribution is observed as expected. **b**, Map of $MCD(0T)$ (left) and $MCD(1T) - MCD(0T)$ (right) for a 60° sample. Only FM contribution is seen. The black and red dashed lines outline the constituent CrI_3 monolayers. The $MCD(0T)$ image was taken after the sample is polarized at $B = 1$ T.



Extended Data Figure 7 | Temperature dependence in natural bilayer CrI_3 . MCD vs magnetic field in a natural bilayer CrI_3 at different temperatures (**a**) and the temperature dependence of the spin flip transition field B_c (**b**). B_c is the average spin-flip transition field between forward and backward sweeps. The error bars are estimated from the width of the transition.



Extended Data Figure 8 | Additional gate-dependent MCD response at 4 K for another sample with $\theta = 1.6^\circ$.